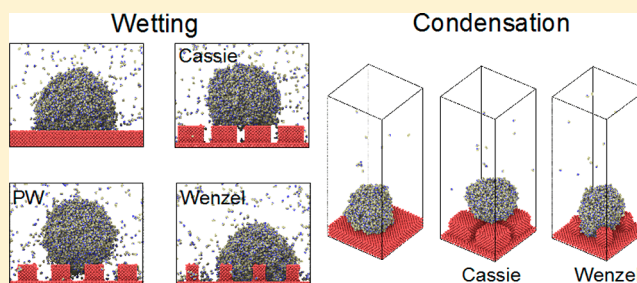


Effects of Solid Fraction on Droplet Wetting and Vapor Condensation: A Molecular Dynamic Simulation Study

Shan Gao, Quanwen Liao, Wei Liu,* and Zhichun Liu*

School of Energy and Power Engineering, Huazhong University of Science and Technology (HUST), Wuhan 430074, China

ABSTRACT: Recently, numerous studies focused on the wetting process of droplets on various surfaces at a microscale level. However, there are a limited number of studies about the mechanism of condensation on patterned surfaces. The present study performed the dynamic wetting behavior of water droplets and condensation process of water molecules on substrates with different pillar structure parameters, through molecular dynamic simulation. The dynamic wetting results indicated that droplets exhibit Cassie state, PW state, and Wenzel state successively on textured surfaces with decreasing solid fraction. The droplets possess a higher static contact angle and a smaller spreading exponent on textured surfaces than those on smooth surfaces. The condensation processes, including the formation, growth, and coalescence of a nanodroplet, are simulated and quantitatively recorded, which are difficult to be observed by experiments. In addition, a wetting transition and a dewetting transition were observed and analyzed in condensation on textured surfaces. Combining these simulation results with previous theoretical and experimental studies will guide us to understand the hypostasis and mechanism of the condensation more clearly.



INTRODUCTION

It is well-known that several physical phenomena occur on surfaces. Consequently, surface morphology and structure and its physicochemical property significantly impact system performance. Superhydrophobic surfaces (SHS) with a composite micronano structure are a result of interactions between living organisms and environments during the long-term evolution process.^{1–4} Superhydrophobic materials attracted increasing attention and were gradually investigated due to their many special properties, such as self-repelling,^{5,6} antisticking,⁷ antifouling,⁸ and self-cleaning,^{3,9,10} which have potential applications in several fields including self-cleaning,⁵ thermal diodes,¹¹ anticing,¹² vapor chambers,¹³ electrostatic energy harvesting,¹⁴ and condensation heat transfer enhancement.¹⁵ Synthetic superhydrophobic surfaces are fabricated through the following two procedures: first micro-nano structures are manufactured with methods of corrosion or photoetching to increase the surface roughness, and subsequently, a thin coating is formed by using a chemical vapor deposition (CVD) method to reduce surface energy.

Recently, superhydrophobic materials with composite micro-nano structure have been increasingly investigated by many scholars, and this has widespread application prospects in actual industry. A large number of experimental studies focused on the behavior of droplets on different textured surfaces in different environment,^{16–19} the studies mainly include the wetting process of droplet^{20,21} and condensation process.^{22–26} Hyeongyun et al.²⁷ proposed a “focal plane shift imaging” technique to studied the effects of droplet mismatch, multidroplet coalescence, and multihop coalescence on droplet jumping speed. This technique resolved the full 3D trajectory of multiple jumping

events and found that the departure angle during droplet jumping is not a function of droplet mismatch or number of droplets coalescing prior to jumping. Shreyas et al.²⁸ combined numerical simulation with experiment to study individual droplet heat transfer on nonwetting surfaces. The results reveal that the majority of heat transfer occurs at the three phases contact line.

Current studies are not limited at the macro-scale level, and the rapid development of molecular simulation provides a valuable research instrument in investigating numerous interfacial phenomena at the microscale level. However, a significant amount of attention focused on the wetting process of droplets on various textured surfaces,^{29–40} there is paucity of studies examining a simulation study of a condensation process on patterned surfaces. There are several gaps in droplet formation, growth, and coalescence processes on textured surfaces when compared with those on a smooth surface. The aim of the present study involved the fore-mentioned differences, and thus the above-mentioned processes were simulated and numerically based on molecular dynamics simulation.

The present study involves visualizing water droplet dynamic wetting behavior and the course of vapor condensation on various silicon surfaces, including smooth surfaces and surfaces featuring various pillared structures. This is followed by obtaining similarities and differences between the aforementioned two processes by comparing smooth surfaces and textured surfaces. With respect to the wetting process, the results indicate that the contact angle of droplets on textured surfaces exceeds those on smooth surfaces and that droplets on a roughened surface exhibit

Received: September 11, 2017

Published: October 5, 2017

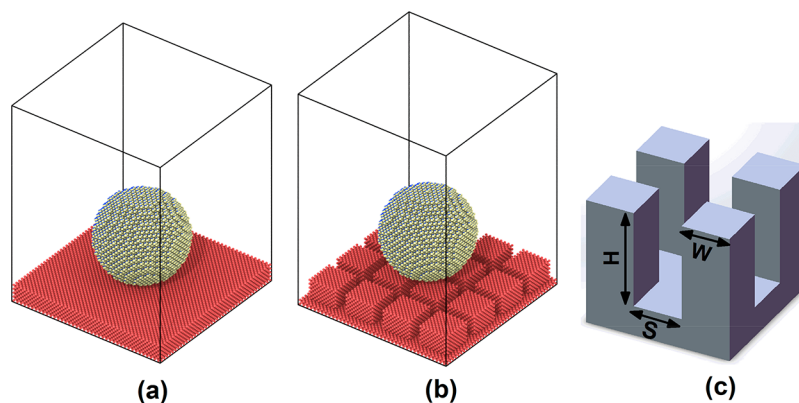


Figure 1. Physical models of wetting simulation on (a) a smooth surface and (b) a textured surface at initial moment, and (c) schematics of the modeled structured surface.

the Cassie state, PW (partially wetted) state, and Wenzel state successively with decreasing solid fraction. With respect to the condensation process, the findings revealed that water molecules are more inclined to gather at the top of nano pillars to form nucleation points on textured surfaces with higher solid fraction, which tend to develop the nonwetting state correspondingly. The formation, growth, and coalescence of a nanodroplet are simulated and quantitatively recorded. In addition, a wetting transition and a dewetting transition were observed and analyzed in condensation on textured surfaces. This study has implications for understanding the detailed behavior and mechanism of condensation on textured surfaces.

MODEL AND METHODOLOGY

Molecular dynamics simulation is used in all simulations to visualize wetting courses of nanodroplets on different textured surfaces and aggregative behavior of water molecules on various textured surfaces in the process of condensation. A large-scale atomic/molecular massively parallel simulator (LAMMPS) package is used to conduct all simulations in which water is considered as a condensation material, and silicon atoms construct the substrate. The building block of the surface includes a diamond lattice consisting of 8 silicon atoms, and the lattice constant of the unit cell corresponds to 5.43 Å. The water region is built with a face-centered cubic unit (FCC) with a different lattice constant that is determined by water density at different temperatures.

Physical Model. In order to study the effects of surface fraction on droplet wetting morphology, six sets of simulations were conducted in the present study including behavior of nanodroplets on a smooth surface and five textured surfaces consisting of a pillar array with height $H = 18.1$ Å, different width W , and different interpillar spacing S (as shown in Figure 1 c). Detailed structure parameters are listed in Table 1. Physical models at initial moment are shown in Figure 1 a,b, horizontal dimensions of all substrates correspond to 142.8 Å \times 142.8 Å, and a spherical water droplet with a diameter of 73.2 Å is placed on the surface.

With respect to the condensation process, the surface is maintained equivalent to that described above, although the length of the simulation box in the z direction is twice that in the horizontal dimension to contain more gaseous water molecules.

Simulation Details. In all simulations, the periodic boundary conditions are only applied in the horizontal direction while the fixed boundary condition and bounce-back boundary condition are applied in the lower and upper boundaries, respectively.

Table 1. Physical Dimensions of Pillars: Width W , Distance between Pillars S , and Height H ^a

	S (Å)	W (Å)	H (Å)	ϕ_s (%)
Structure 1	—	—	—	100
Structure 2	9.04	27.11	18.1	56.24
Structure 3	12.65	23.49	18.1	42.23
Structure 4	16.27	19.88	18.1	30.24
Structure 5	19.88	16.27	18.1	20.26
Structure 6	23.49	12.65	18.1	12.25

^aStructural properties of rough surfaces: solid fraction $\phi_s = W^2 / (W + S)^2$.

The computational domain is divided into three regions, namely, vapor, liquid, and solid regions. Both vapor and liquid regions are filled with water molecules, and the solid region corresponds to a silica surface. With respect to water, the TIP4P model is adopted by several researchers; most studies consider that the TIP4P model of water is effective and approximate⁴¹ and proved the model accuracy by using an equation of state (EOS). Hence, the TIP4P model is used in the present study. The TIP4P models have four interaction points that are obtained by adding a dummy atom near the oxygen atom along the bisector of the HOH angle of the 3-site models. The dummy atom only includes a negative charge, and the oxygen atom only includes mass. The model improves electrostatic distribution around the water molecule. The potential for the TIP4P model is represented by the following expression:

$$U = 4\epsilon_{OO} \left[\left(\frac{\sigma_{OO}}{r_{ia}r_{jb}} \right)^{12} - \left(\frac{\sigma_{OO}}{r_{ia}r_{jb}} \right)^6 \right]_{a=1,b=1} + \sum_{a=1}^3 \times \sum_{b=1}^3 \frac{q_{ia}q_{jb}}{4\epsilon_0} \frac{1}{r_{ia}r_{jb}} \quad (1)$$

where i and j denote different water molecules, and a and b denote different interaction sites in a water molecule. Additionally, a and b possess three identical numeric values, which are defined as oxygen atoms, hydrogen atoms, and dummy atoms when their values correspond to 1, 2, and 3, respectively. Furthermore, $r_{ia}r_{jb}$ corresponds to the distance between two interaction sites of a and b in water molecules, and the interaction sites could be located on the atoms or on dummy sites. The first term in the above formula corresponds to the 12–6 type Lennard-Jones potential, which represents the van der Waals nonbonding

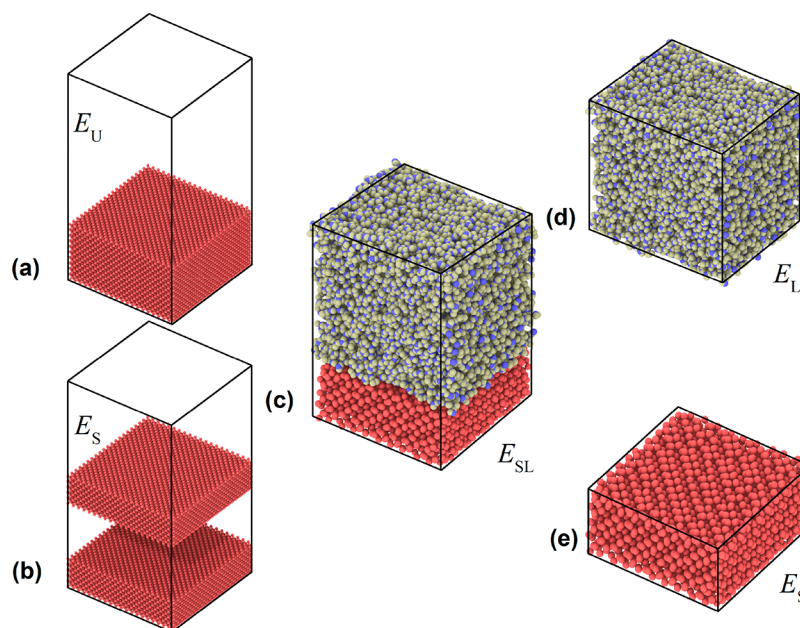


Figure 2. An illustration of the calculation of the surface tension for a surface using two boxes with (a) unified surfaces and (b) separated surfaces. The calculation of the silicon–water interface tension by using three boxes with (c) a silicon–water interface, (d) pure water, and (e) pure silicon.

force between two water molecules. The Lennard-Jones term only applies to the interaction between the oxygen atoms. Moreover, σ and ϵ correspond to LJ potential parameters with ϵ corresponding to the interaction energy well-depth, and σ corresponding to the finite distance where the LJ potential corresponds to zero. The second term represents electrostatic interaction with ϵ_0 denoting vacuum permittivity, q_{ia} denoting the charge of an interaction site of a in the i th water molecule, and q_{jb} denoting the charge of the interaction site of b in the j th water molecule in a similar manner. Additionally, the bond distance and bond angle for water molecules are fixed by using the Shake algorithm throughout the MD simulations.

The force between every silica atoms is implemented by using the SW potential, and the form is shown as follows:

$$E = \sum_i \sum_{j>1} \phi_2(r_{ij}) + \sum_i \sum_{j \neq i} \sum_{k>j} \phi_3(r_{ij}, r_{jk}, \theta_{ijk}) \quad (2)$$

where ϕ_2 represents a two-body term and ϕ_3 denotes a three-body term. The summations in the formula are over all neighbors j and k of atom i within a cutoff distance.

The interaction parameter between surface atoms and water molecules is calculated by using the Lorentz–Berthelot mixing rules as follows:

$$\epsilon_{ij} = \sqrt{\epsilon_i \epsilon_j} \quad (3)$$

$$\sigma_{ij} = (\sigma_i + \sigma_j)/2 \quad (4)$$

where i and j represent different atom species, and only surface-oxygen LJ interactions are calculated in a manner similar to the TIP4P water model. The processing of the surface is as follows: several layers on the bottom of substrate are fixed around their original positions to prevent atoms from penetration, and remaining layers are applied from the thermostat to heating surface. A cutoff distance of 10 Å is used for LJ and electrostatic interaction calculations, and the electrostatic interactions are incorporated with a particle mesh Ewald method to evaluate the long-range effect.

A time step of 1 fs is adopted in all cases. The simulations of wetting courses are performed in the following two stages: water molecules are equilibrated with Nose–Hoover thermostat in an NVT ensemble until the temperature of water achieves a stable value of 298 K, and the substrate is simultaneously heated to 298 K with a Langevin thermostat in an NVE ensemble. This is followed by removing the thermostat that is applied on the water molecules. The NVE ensemble is used for the water, and the water droplet subsequently begins to spread on the surface.

Similar reactions are involved in a process in which gaseous water molecules condense on different surfaces, and the only difference involves water temperature that is initially controlled at a stable value of 363 K. Additionally, a circle is introduced to ensure that the presence of sufficient gaseous water molecules forms droplets as follows: the general condensation of a specific number of water molecules on a surface causes another set of water molecules to be appended to the gas phase space and the processing steps of newly added molecules completely correspond to the fore-mentioned steps.

Furthermore, surface tension and interface tension are calculated in the following manner.⁴² Solid–vapor surface tension γ_{SV} is computed based on two NVT simulations, namely, using models with and without two additional surfaces (as shown in Figure 2a,b). Each of the boxes possesses the same dimensions, contains the same number of atoms, and is subjected to NVT molecular dynamics simulation at 298 K for 1000 ps. The difference in average total energy between the separated structure E_S and the unified structure E_U is equal to the cleavage energy per surface area $2A$, and the surface tension γ_{SV} is expressed as follows:

$$\gamma_{SV} = \frac{E_S - E_U}{2A} - T \frac{S_S - S_U}{2A} \approx \frac{E_S - E_U}{2A} \quad (5)$$

The entropy contribution $-T(S_S - S_U)/2A$ is negligible when compared to the cohesive energy contribution $(E_S - E_U)/2A$. Analogously, water–vapor surface tension is calculated in the fore-mentioned manner.



Figure 3. An illustration of the spreading progression of water nanodroplets on the silicon substrate with different structures and solid fractions (front view).

As shown in Figure 2c,d,e, solid–water interface tension γ_{SL} is computed in a similar manner based on three NVT simulations. The difference in average energies, and E_{SL} , E_L , and E_S yields the interfacial energy $(E_{SL} - E_S - E_L)/2A$, and the interface tension is as follows:

$$\gamma_{SL} = \frac{E_{SL} - E_S - E_L}{2A} - T \frac{S_{SL} - S_S - S_L}{2A} \quad (6)$$

The entropy contribution in the formula cannot be ignored, and it is approximately equal to $0.06 \pm 0.03 \text{ J/m}^2$.

RESULTS AND DISCUSSION

Dynamic Wetting. The snapshots shown in Figure 3 illustrate morphological changes in droplets from initial states to stable states for the six systems. The droplets exhibit the Cassie state on surfaces with higher surface fraction (Structure 2 and Structure 3) because the smaller gaps limit the number of water

molecules that move down between the pillars. The transition from the Cassie state to the Wenzel state occurs with decreases in the pillar surface fraction as follows: droplets exhibit the PW state in Structure 4 and Structure 5, and the droplets finally exhibit the Wenzel state in Structure 6.

The static contact angles of water droplets on each surface are first computed to measure wettability of different surfaces. The density of a water droplet is defined as the number of water molecules in a unit cubic cell and the boundary between liquid and vapor for a given droplet is determined at the position in which the density corresponds to half the bulk water density. The density contour of droplet is shown in Figure 4a. A density profile along the centerline of the water droplet is described in Figure 4b, and the solid line denotes the fit using the hyperbolic function. The coordinates of the atoms that are near the liquid–gas interface were extracted to fit a curve, and a contact angle was obtained by computing the slope of tangent line at a three-phase contact point as shown in Figure 4c. The solid fraction is

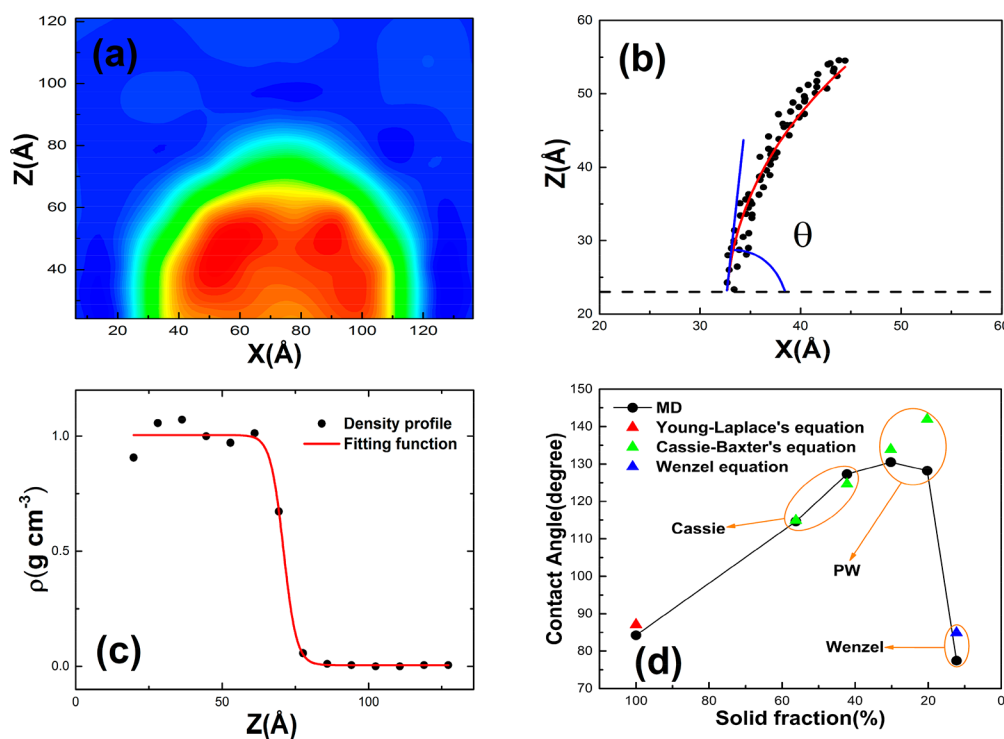


Figure 4. Measurement of the static contact angle. (a) Density contours of water droplets. (b) Black points denote atoms near the gas–liquid interface to characterize the surface of droplet, the red curve is a fit to the black points, and the blue curve denotes the contact angle. (c) Density profile along the centerline of the water droplet. The red line corresponds to the fit using the hyperbolic function. (d) The dependency of the theoretical and numerical values of the contact angle with respect to the solid fraction in which circles denote the numerical values and triangles denote the theoretical values.

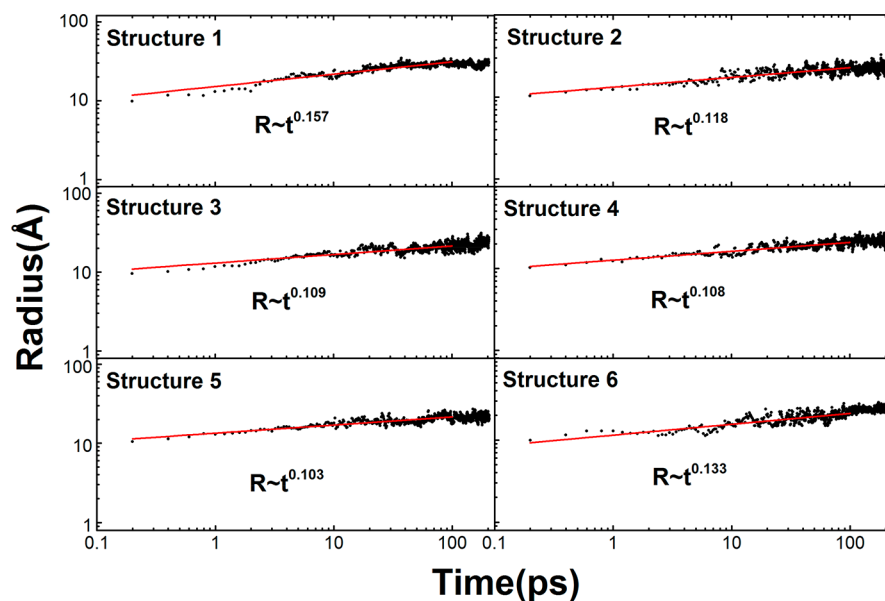


Figure 5. Simulative values of the spreading radius that are plotted as a function of time for different substrates in which black points denote the simulation value and the red curve is a fit to the black points.

determined by the geometry structure parameters such that it is possible to obtain the state of change in the contact angle with respect to the solid fraction (as shown in Figure 4d).

Simultaneously, the contact angle computed by the theoretical formula is used as a standard of comparison as follows: the contact angle can be obtained based on Young's equation for a droplet on a smooth surface:⁴³ $\cos \theta_0 = \frac{\gamma_{SV} - \gamma_{SL}}{\gamma_{LV}}$. With respect to a rough surface, the apparent contact angle for Wenzel state,

PW state, and Cassie state is calculated by using the following formula separately:^{44,45}

$$\cos \theta_W = r_w \cos \theta_0 \quad (7)$$

$$\cos \theta_C = \phi_S \cos \theta_0 + \phi_S - 1 \quad (8)$$

Specifically, r_w denotes the roughness ratio of the total surface area in contact with liquid over the projected area in the penetrated Wenzel state, and ϕ_S denotes the fraction of the

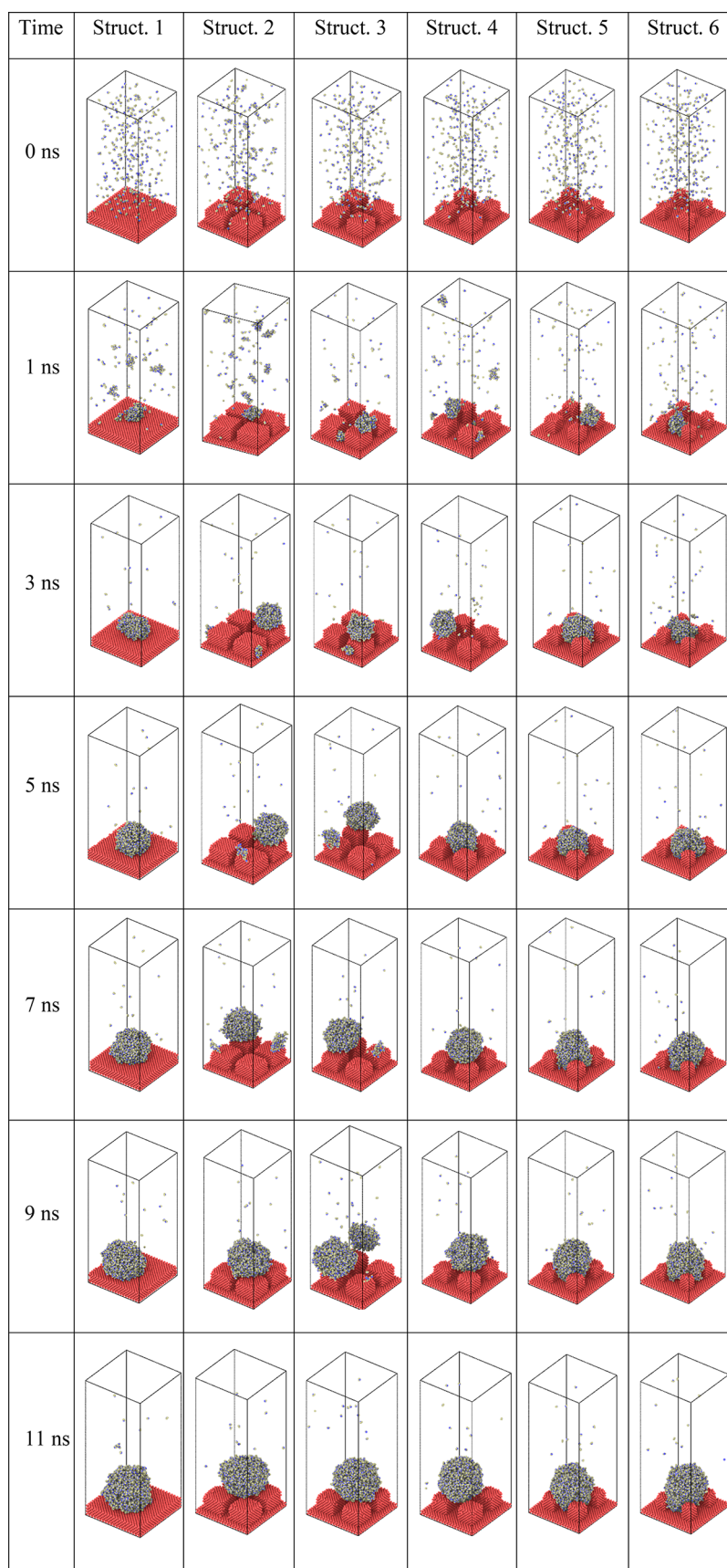


Figure 6. Condensation process of water molecules on the silicon substrate with different structures and solid fractions (orthogonal perspective).

solid surface in contact with liquid in the Cassie state and PW state. As previously mentioned, the surface intension and

interface tension used in the above formula are computed by the excess free energy method, and their concrete values correspond

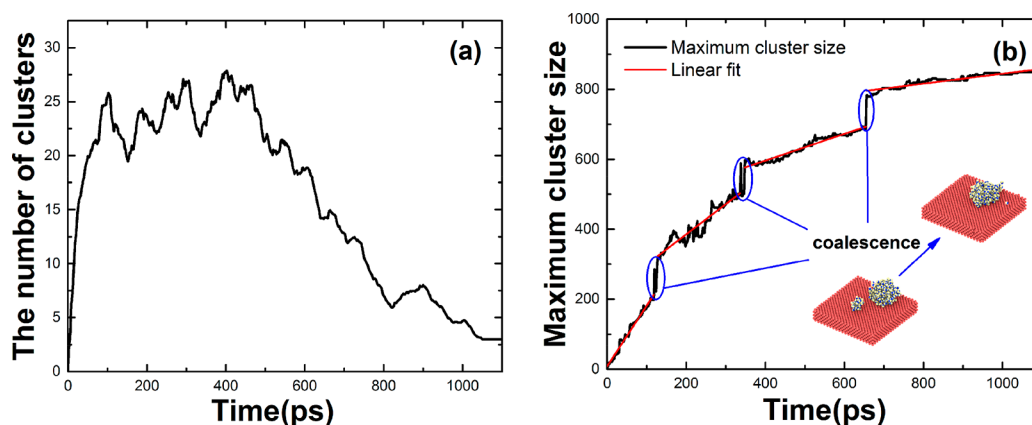


Figure 7. Evolution of the number of clusters and growth of the maximum cluster size on the surface.

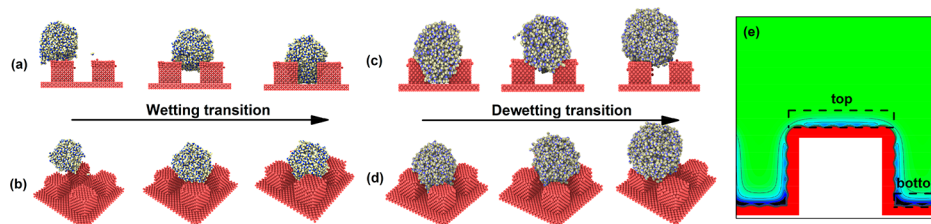


Figure 8. Wetting transition on the silicon substrate (Structure 4): (a) front view; (b) orthogonal view. Dewetting transition on the silicon substrate (Structure 4): (c) front view; (d) orthogonal view. (e) An equipotential curve of potential function between water molecules and textured surface (Structure 4).

to $\gamma_{SV} = 1.3504$ N/m, $\gamma_{SL} = 1.3442$ N/m, and $\gamma_{LV} = 0.0614$ N/m at 298 K.

As observed above, a liquid droplet on a roughened surface can exhibit a Cassie state, PW state, and Wenzel state successively with a decreasing solid fraction. However, the Cassie state corresponds to the preferred hydrophobic state in which a droplet possesses a much smaller contact angle hysteresis and therefore a higher mobility. This state is guaranteed by increasing the pillar surface fraction.

The change of spreading radius with respect to time is recorded for different substrates in the slower spreading stage. The spreading exponent is obtained by a linear fit as shown as Figure 5. It is observed that the spreading radius is expressed as the power law of spreading time, $R(t) \sim t^\alpha$, in which α denotes the spreading exponent, and a droplet on the textured surface has a smaller spreading exponent when compared to that on the smooth surface. The spreading exponents of all surfaces are close to $1/7$ in MKT.⁴⁶

Condensation. The condensation processes are implemented on various surfaces with decreasing pillar surface fraction. Typical time-lapse images of each case are shown in Figure 6.

With respect to a smooth surface, the water molecules can be slowed down during the condensation process after they impact with surface atoms. The kinetic energy decreases accordingly, and the aggregation of low energy molecules provides a favorable environment for the formation of clusters on the surface.

With respect to textured surfaces, gaseous water molecules tend to gather on the top of pillars to form clusters, and the clusters merge and grow into droplets that invariably correspond to the Cassie state (Structure 2 and Structure 3). Thus, the decrease in the fraction of the solid surface is accompanied by an increasing number of water molecules that collect at the bottom of pillars to form clusters. As a result, droplets that consist of

grown-up clusters gradually transform into the Wenzel state (Structure 5 and Structure 6).

The formation and coalescence of clusters are observed across all condensation processes. The change of clusters on smooth surfaces is demonstrated in Figure 7a, and observations indicate that the number of clusters increases rapidly in the initial stage and decreases gradually due to coalescence. As shown in Figure 7b, the findings reveal that the cluster size is proportional to time in the growth stage, and the growth of cluster size becomes slower as time progresses. This is followed by an abrupt increase due to the coalescence of clusters.

The droplets that formed on the surface migrated randomly around certain areas as opposed to stabilizing on a specific location (Structure 2 and Structure 3). This is because the interactions exerted on droplets by vapor molecules were asymmetric due to the relatively low vapor density. Hence, the random forces that were provided by the impacting vapor molecules actually drove the droplets to migrate slightly. However, the droplets that formed between the pillars stabilized on a specific location due to the significantly high resistance between the substrate and water. These results suggest that the mobility of the Cassie state exceeds that of the Wenzel state.

Wetting transition and dewetting transition of dropwise condensation on textured surfaces are observed in Structure 4. As shown in the Figure 8a,b, at the beginning, a few water molecules collected on the top of pillars to form droplets in Cassie state, and subsequently, the droplets slid into the valley of the pillars to exhibit the Wenzel state. The diameter of a droplet is smaller than the spacing between pillars, and it is expected to stay at the valley of the pillars when the droplet grows to a size that is comparable to the structure spacing scale. The droplet then begins to interact with the pillars confining it and fills the unit cell to the top of the structures. However, the gap between the neighboring pillars is filled when the size of the droplet exceeds

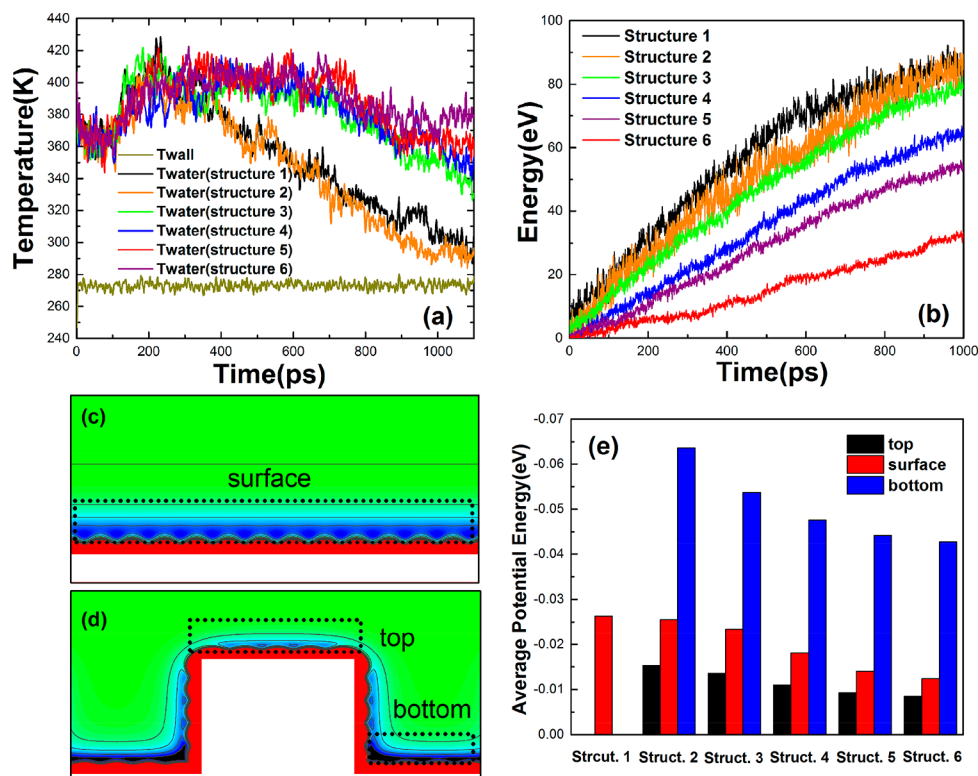


Figure 9. (a) Evolution of vapor temperature during the condensation process on various surfaces. (b) Total heat transfer accumulation with respect to time for surfaces with different solid fractions. (c) Equipotential curve of potential between water molecules and smooth surface. (d) Equipotential curve of potential between water molecules and textured surface. (e) The average potential energy of a water molecule in different regions.

$2^{1/2}S$, and the droplet is squeezed by the surrounding four pillars and deforms naturally away from a spherical shape. A distinct phenomenon occurs when the droplet in the valley continues to grow, namely, a dewetting transition gradually occurs, which is shown in Figure 8c,d. This causes the droplet to remain on the top of four pillars. Additionally, the droplet possesses a higher contact angle. This simulative dewetting transition have been confirmed by past experiments. Zhang Bo et al.⁴⁷ perform experiments, theoretical analysis, and lattice Boltzmann simulations of droplet condensation on a patterned superhydrophobic surface and demonstrate that the dewetting energy barrier can be reduced by manipulating the adhesion forces.

An equipotential curve of potential between water molecules and textured substrate (Structure 4) are mapped in Figure 8e, which helps us to analyze the aforementioned wetting and dewetting transition from the point of the potential energy. The region near the top of pillars and the region near the valley of pillars are defined as top region and bottom region, respectively. Both of them are regions with low potential energy. The water molecules prefer to gather at the bottom region, because the bottom region has a lower potential energy. At the beginning of condensation, water molecules more easily gather on the top and form droplets, because the top of the pillars is closer to the gas phase region. As the droplet size exceeds the top region, more and more water molecules move to the bottom region due to the lower potential energy in bottom region. It leads to the droplet slide into the valley of the pillars, namely, the occurrence of wetting transition. Subsequently, with the sustained growth of droplet, the valley of the pillars is filled up with water molecules, and then the new liquid water molecules will gather on the top of droplet. The increasing water molecules in top region will gradually pull the bottom water molecules out of the valley of

pillars, namely, a dewetting transition occurs. Finally, the droplet is inclined to stay on the top of pillars with sublowest potential energy and exhibit a Cassie state.

Figure 9a shows the evolution of vapor temperature during condensation process on various surfaces. The findings indicate that vapor temperature decrease rapidly and linearly. Furthermore, the heat exchange between the water vapor and the cold wall is calculated as shown in Figure 9b. The accumulation of heat transfer is calculated for six cold walls with different solid surface fractions. The results reveal that all the six curves generally exhibit linearity, and this illustrates that the heat flux that is defined as the ratio of the slope of each curve to the cold surface area is constant during condensation process. The results indicate that the smooth surface (Structure 1) and the textured surface with higher solid fraction (Structure 2) exhibit a higher heat transfer performance when compared to the textured surfaces with lower solid fractions, which is different from previous experiments. To explain this contradictory phenomenon and elucidate the underlying mechanism, equipotential curves between water molecules and different substrate are shown in Figure 9c,d. We calculated the average potential of a water molecule when located in three different regions, namely surface region, top region, and bottom region. The results in Figure 9e show that the average potential of a water molecule in surface region increase with decreasing solid fraction. Therefore, for a single water molecule, the quantity of heat released during condensation process will reduce. In our simulations, the number of water molecules is constant, which leads to surface with higher solid fraction exhibit a higher heat transfer performance. However, there is unlimited amount of water molecules in those experiments. The water mass flow of the MD simulations herein is obviously different from that of those experiments. In addition,

the droplets on textured surfaces can be removed from the surface more easily due to higher average potential, coalescence-induced jump or gravity. The higher mass flow of phase-changed water molecules on textured surfaces than that on a smooth surface may lead to high heat transfer performance of textured surfaces.

CONCLUSIONS

In this work we applied molecular dynamics simulation to investigate the effects of solid fraction on droplet wetting and vapor condensation, showing that droplets exhibit the Cassie state on textured surfaces with a high fraction of solid surface and gradually transforms into the Wenzel state when the fraction of the solid surface decreases. The droplets possess a higher static contact angle and a smaller spreading exponent on textured surfaces than those on smooth surfaces. Furthermore, in the condensation, droplets nucleation, growth and coalescence processes were all visualized and quantitatively recorded at the molecular level, and we showed that the wetting transition and dewetting transition were caused by the inhomogeneity of water molecules potential energy on textured surfaces. We will understand the mechanism of the droplet wetting and condensation more clearly through a combination of this simulation's outcomes and previous theoretical and experimental studies.

AUTHOR INFORMATION

Corresponding Authors

*E-mail: w_liu@hust.edu.cn (WL).

*E-mail: zcliu@hust.edu.cn (ZCL).

Author Contributions

S.G. carried out the MD calculations. Q.L., Z.L., and W.L. supervised the research. All authors analyzed the calculation data and edited the manuscript.

Notes

The authors declare no competing financial interest.

ACKNOWLEDGMENTS

This project was supported by the National Natural Science Foundations of China: No.51736004 and No.51776079. The study was performed at the National Supercomputer Center in Tianjin, and the calculations were performed on TianHe-1(A).

REFERENCES

- (1) Barthlott, W.; Neinhuis, C. Purity of the sacred lotus, or escape from contamination in biological surfaces. *Planta* **1997**, *202* (1), 1–8.
- (2) Gao, X.; Jiang, L. Biophysics: water-repellent legs of water striders. *Nature* **2004**, *432* (7013), 36.
- (3) Neinhuis, C.; Barthlott, W. Characterization and Distribution of Water-repellent, Self-cleaning Plant Surfaces. *Ann. Bot.* **1997**, *79* (6), 667–677.
- (4) Watson, G. S.; Watson, J. A. Natural nano-structures on insects—possible functions of ordered arrays characterized by atomic force microscopy. *Appl. Surf. Sci.* **2004**, *235* (1–2), 139–144.
- (5) Fürstner, R.; Barthlott, W.; Neinhuis, C.; Walzel, P. Wetting and Self-Cleaning Properties of Artificial Superhydrophobic Surfaces. *Langmuir* **2005**, *21* (3), 956–961.
- (6) Blossley, R. Self-cleaning surfaces—virtual realities. *Nat. Mater.* **2003**, *2* (5), 301–6.
- (7) Boreyko, J. B.; Chen, C. H. Self-propelled dropwise condensate on superhydrophobic surfaces. *Phys. Rev. Lett.* **2009**, *103* (18), 184501.
- (8) Miwa, M.; Nakajima, A.; Fujishima, A.; Hashimoto, K.; Watanabe, T. Effects of the Surface Roughness on Sliding Angles of Water Droplets on Superhydrophobic Surfaces. *Langmuir* **2000**, *16* (13), 5754–5760.

- (9) Miljkovic, N.; Enright, R.; Nam, Y.; Lopez, K.; Dou, N.; Sack, J.; Wang, E. Jumping-Droplet-Enhanced Condensation on Scalable Superhydrophobic Nanostructured Surfaces. *Nano Lett.* **2013**, *13* (1), 179.
- (10) Richard, D.; Quéré, D. Viscous drops rolling on a tilted non-wettable solid. *Epl* **1999**, *48* (3), 286.
- (11) Boreyko, J. B.; Zhao, Y.; Chen, C.-H. Planar jumping-drop thermal diodes. *Appl. Phys. Lett.* **2011**, *99* (23), 234105.
- (12) Cao, L.; Jones, A. K.; Sikka, V. K.; Wu, J.; Gao, D. Anti-icing superhydrophobic coatings. *Langmuir* **2009**, *25* (21), 12444–8.
- (13) Boreyko, J. B.; Chen, C.-H. Vapor chambers with jumping-drop liquid return from superhydrophobic condensers. *Int. J. Heat Mass Transfer* **2013**, *61*, 409–418.
- (14) Miljkovic, N.; Preston, D. J.; Enright, R.; Wang, E. N. Electrostatic charging of jumping droplets. *Nat. Commun.* **2013**, *4*, 2517.
- (15) Li, G.; Alhosani, M. H.; Yuan, S.; Liu, H.; Ghaferi, A. A.; Zhang, T. Microscopic droplet formation and energy transport analysis of condensation on scalable superhydrophobic nanostructured copper oxide surfaces. *Langmuir* **2014**, *30* (48), 14498–511.
- (16) Subramanyam, S. B.; Kondrashov, V.; Ruhe, J.; Varanasi, K. K. Low Ice Adhesion on Nano-Textured Superhydrophobic Surfaces under Supersaturated Conditions. *ACS Appl. Mater. Interfaces* **2016**, *8* (20), 12583–7.
- (17) Dietz, C.; Rykaczewski, K.; Fedorov, A. G.; Joshi, Y. Visualization of droplet departure on a superhydrophobic surface and implications to heat transfer enhancement during dropwise condensation. *Appl. Phys. Lett.* **2010**, *97* (3), 033104.
- (18) Olceroglu, E.; McCarthy, M. Self-Organization of Microscale Condensate for Delayed Flooding of Nanostructured Superhydrophobic Surfaces. *ACS Appl. Mater. Interfaces* **2016**, *8* (8), 5729–36.
- (19) Rykaczewski, K.; Scott, J. H. J.; Rajauria, S.; Chinn, J.; Chinn, A. M.; Jones, W. Three dimensional aspects of droplet coalescence during dropwise condensation on superhydrophobic surfaces. *Soft Matter* **2011**, *7* (19), 8749–8752.
- (20) Callies, M.; Chen, Y.; Marty, F.; Pépin, A.; Quéré, D. Microfabricated textured surfaces for super-hydrophobicity investigations. *Microelectron. Eng.* **2005**, *78–79*, 100–105.
- (21) Choi, W.; Tuteja, A.; Mabry, J. M.; Cohen, R. E.; McKinley, G. H. A modified Cassie-Baxter relationship to explain contact angle hysteresis and anisotropy on non-wetting textured surfaces. *J. Colloid Interface Sci.* **2009**, *339* (1), 208–16.
- (22) Boreyko, J. B.; Chen, C. H. Self-propelled dropwise condensate on superhydrophobic surfaces. *Phys. Rev. Lett.* **2009**, *103* (18), 184501.
- (23) Chen, X.; Wu, J.; Ma, R.; Hua, M.; Koratkar, N.; Yao, S.; Wang, Z. Nanograsped Micropyramidal Architectures for Continuous Dropwise Condensation. *Adv. Funct. Mater.* **2011**, *21* (24), 4617–4623.
- (24) He, M.; Ding, Y.; Chen, J.; Song, Y. Spontaneous Uphill Movement and Self-Removal of Condensates on Hierarchical Tower-Like Arrays. *ACS Nano* **2016**, *10* (10), 9456–9462.
- (25) Leach, R. N.; Stevens, F.; Langford, S. C.; Dickinson, J. T. Dropwise Condensation: Experiments and Simulations of Nucleation and Growth of Water Drops in a Cooling System. *Langmuir* **2006**, *22* (21), 8864–8872.
- (26) Varanasi, K. K.; Hsu, M.; Bhate, N.; Yang, W.; Deng, T. Spatial control in the heterogeneous nucleation of water. *Appl. Phys. Lett.* **2009**, *95* (9), 094101.
- (27) Cha, H.; Chun, J. M.; Sotelo, J.; Miljkovic, N. Focal Plane Shift Imaging for the Analysis of Dynamic Wetting Processes. *ACS Nano* **2016**, *10* (9), 8223–32.
- (28) Chavan, S.; Cha, H.; Orejon, D.; Nawaz, K.; Singla, N.; Yeung, Y. F.; Park, D.; Kang, D. H.; Chang, Y.; Takata, Y.; Miljkovic, N. Heat Transfer through a Condensate Droplet on Hydrophobic and Nanostructured Superhydrophobic Surfaces. *Langmuir* **2016**, *32* (31), 7774–87.
- (29) Giovambattista, N.; DeBenedetti, P. G.; Rossky, P. J. Effect of surface polarity on water contact angle and interfacial hydration structure. *J. Phys. Chem. B* **2007**, *111* (32), 9581–9587.

- (30) Hong, S. D.; Ha, M. Y.; Balachandar, S. Static and dynamic contact angles of water droplet on a solid surface using molecular dynamics simulation. *J. Colloid Interface Sci.* **2009**, *339* (1), 187–95.
- (31) Kaware, R.; Desai, S. Molecular dynamics modeling of water nanodroplet spreading on topographically patterned silicon dioxide and silicon nitride substrates. *IEEE Transactions* **2015**, *47* (7), 767–782.
- (32) Khan, S.; Singh, J. K. Wetting transition of nanodroplets of water on textured surfaces: a molecular dynamics study. *Mol. Simul.* **2014**, *40* (6), 458–468.
- (33) Koishi, T.; Yasuoka, K.; Fujikawa, S.; Ebisuzaki, T.; Zeng, X. C. Coexistence and transition between Cassie and Wenzel state on pillared hydrophobic surface. *Proc. Natl. Acad. Sci. U. S. A.* **2009**, *106* (21), 8435–40.
- (34) Koishi, T.; Yasuoka, K.; Fujikawa, S.; Zeng, X. C. Measurement of contact-angle hysteresis for droplets on nanopillared surface and in the Cassie and Wenzel states: a molecular dynamics simulation study. *ACS Nano* **2011**, *5* (9), 6834–6842.
- (35) Lu, G.; Duan, Y. Y.; Wang, X. D. Effects of Free Surface Evaporation on Water Nanodroplet Wetting Kinetics: A Molecular Dynamics Study. *J. Heat Transfer* **2015**, *137* (9), 091001.
- (36) Niu, D.; Tang, G. H. Static and dynamic behavior of water droplet on solid surfaces with pillar-type nanostructures from molecular dynamics simulation. *Int. J. Heat Mass Transfer* **2014**, *79*, 647–654.
- (37) Niu, D.; Tang, G. H. The effect of surface wettability on water vapor condensation in nanoscale. *Sci. Rep.* **2016**, *6*, 19192.
- (38) Prakash, S.; Xi, E.; Patel, A. J. Spontaneous recovery of superhydrophobicity on nanotextured surfaces. *Proc. Natl. Acad. Sci. U. S. A.* **2016**, *113* (20), 5508.
- (39) Savoy, E. S.; Escobedo, F. A. Molecular simulations of wetting of a rough surface by an oily fluid: effect of topology, chemistry, and droplet size on wetting transition rates. *Langmuir* **2012**, *28* (7), 3412–9.
- (40) Zhang, Z.; Matin, M. A.; Ha, M. Y.; Jang, J. Molecular Dynamics Study of the Hydrophilic-to-Hydrophobic Switching in the Wettability of a Gold Surface Corrugated with Spherical Cavities. *Langmuir* **2016**, *32* (37), 9658–63.
- (41) Zielkiewicz, J. Structural properties of water: comparison of the SPC, SPCE, TIP4P, and TIP5P models of water. *J. Chem. Phys.* **2005**, *123* (10), 104501.
- (42) Heinz, H.; Vaia, R. A.; Farmer, B. L.; Naik, R. R. Accurate Simulation of Surfaces and Interfaces of Face-Centered Cubic Metals Using 12–6 and 9–6 Lennard-Jones Potentials. *J. Phys. Chem. C* **2008**, *112* (44), 17281–17290.
- (43) Young, T. An Essay on the Cohesion of Fluids. *Philos. Trans. R. Soc. London* **1805**, 65–87.10.1098/rstl.1805.0005
- (44) Cassie, A. B. D.; Baxter, S. Wettability of porous surfaces. *Trans. Faraday Soc.* **1944**, *40*, 546–551.
- (45) Wenzel, R. N. RESISTANCE OF SOLID SURFACES TO WETTING BY WATER. *Ind. Eng. Chem.* **1936**, *28* (8), 988–994.
- (46) Blake, T. D.; Haynes, J. M. Kinetics of liquid/liquid displacement. *J. Colloid Interface Sci.* **1969**, *30* (3), 421–423.
- (47) Zhang, B.; Chen, X.; Dobnikar, J.; Wang, Z.; Zhang, X. Spontaneous Wenzel to Cassie dewetting transition on structured surfaces. *Physical Review Fluids* **2016**, *1* (7), 073904.